Photochemical & Photobiological Sciences (2025) 24:1107–1126
https://doi.org/10.1007/s43630-025-00754-3

ORIGINAL PAPERS

TiO_2@ZIF-8 hybrid as a type II heterojunction photocatalyst:adsorption/photocatalytic properties, kinetics, and effect of humidity

A. Neren Ökte[1] · **Duygu Tuncel**[1,2]

Received: 5 February 2025 / Accepted: 20 June 2025 / Published online: 4 July 2025
© The Author(s) 2025

Abstract

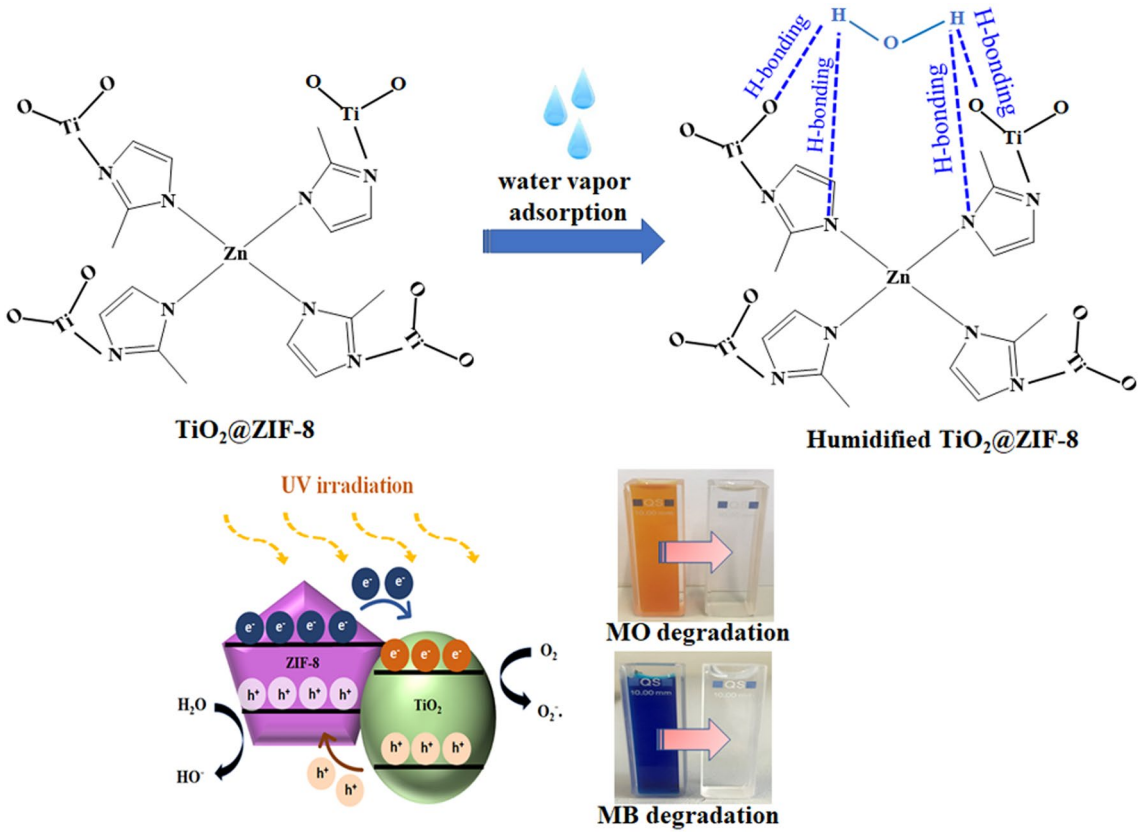
TiO_2@ZIF-8 hybrid and its humidified forms are synthesized as type 2 heterojunction systems using a facile sol–gel method at different relative humidity (RH) conditions. The hybrids' surface characteristics and optical properties are thoroughly examined, followed by investigations into adsorption capacities and photocatalytic activities using anionic-methyl orange (MO) and cationic-methylene blue (MB) dyes. TiO_2@ZIF-8 hybrid generates a mesoporous structure with a higher surface area (135.6 $m^2\ g^{-1}$) than bare TiO_2 (40.1 $m^2\ g^{-1}$). Band gap energies of TiO_2@ZIF-8 (3.00 eV) and humidified hybrids (2.95–2.91 eV) decrease compared to the individual phases of TiO_2 (3.08 eV) and ZIF-8 (4.9 eV). XPS analysis verifies the electron donation from ZIF-8 to TiO_2. Adsorptions of MO and MB differ depending on the affinities of MO or MB's functional groups on the TiO_2@ZIF-8 and humidified hybrids. TiO_2@ZIF-8 demonstrates 98.7% MO and 89.5% MB degradations within 100 min irradiation. Dark adsorption studies follow Langmuir model with Langmuir constants of $K_L = 0.445$ L mg^{-1} for MO in the presence of TiO_2@ZIF-8 and $K_L = 0.409$ L mg^{-1} for MB in the presence of TiO_2@ZIF-8 (84% RH). Meanwhile, pseudo-second-order kinetic model is applicable for dark experiments with rate constants of $k_2 = 0.918$ g $mg^{-1}\ min^{-1}$ for MO in the existence of TiO_2@ZIF-8 and $k_2 = 0.917$ g $mg^{-1}\ min^{-1}$ for MB in the existence of TiO_2@ZIF-8 (84% RH). Under irradiation, TiO_2@ZIF-8 (84% RH) has higher first-order rate constant '*k*' values for both MO (0.0134 min^{-1}) and MB (0.0146 min^{-1}) relative to that of TiO_2@ZIF-8 (0.0129 min^{-1} for MO and 0.0112 min^{-1} for MB). Based on Langmuir–Hinshelwood model, TiO_2@ZIF-8 (84% RH)) shows the highest adsorption coefficients (*K*) of 0.164 L mg^{-1} for MO and 0.192 L mg^{-1} for MB and rate constants (*k*) of 0.197 mg $L^{-1}\ min^{-1}$ for MO and 0.182 mg $L^{-1}\ min^{-1}$ for MB. Notably, the hybrids maintain high stability and photocatalytic efficiency after four consecutive degradation cycles, highlighting their potential for sustainable environmental remediation.

✉ A. Neren Ökte
okteayse@bogazici.edu.tr

[1] Department of Chemistry, Boğaziçi University, 34342 Bebek, Istanbul, Turkey

[2] Department of Analytical Chemistry, Faculty of Pharmacy, Fenerbahçe University, 34758 Ataşehir, Istanbul, Turkey

Graphical abstract



Keywords Hybrid photocatalysts · Relative humidity (RH) · Dye adsorption · Photoactvity · Kinetic analysis

1 Introduction

Photocatalyst design is crucial to develop highly efficient and feasible materials [1]. Recent studies, hence, have focused on new photocatalysts with more than one phase. [2–6]. Among these, hybrid materials lead to the establishment of synergy between the constituents and ultimately, promote the overall efficiency of the process. TiO_2 holds significant applications in photocatalytic degradation processes owing to its unique light-harvesting properties, high stability, low processing costs, and non-toxicity [7]. However, its efficiency is limited due to nanoparticle aggregation and rapid recombination of photoinduced electron–hole pairs [8]. Therefore, incorporating TiO_2 with appropriate materials like metal–organic frameworks (MOFs) to overcome its drawbacks and maximize its performance is an expanding research area. MOF structures involve center-metal ion(s) and organic ligand groups [9]. They possess a higher surface area and a porous nature [10]. In light-responsive MOFs, ligand groups may serve as an antenna and supply electron migration from the ligands to the metal site [11, 12]. Nevertheless, their photo-activities under UV irradiation cannot reach the quality of traditional photo-catalysts due to their high band-gap energies. Zeolitic imidazolate framework-8 (ZIF-8) is constructed with tetrahedral units of Zn^{2+} metal centers and N atoms of imidazolate anions [13]. The heterojunction that can be established between ZIF-8 and TiO_2 limits the disadvantages of individual usage and boosts photocatalytic performances by accelerating charge transfer [14–17].

Chandra et al. prepared TiO_2@ZIF-8 composite with high thermal stability [18]. The composite exhibited degradation rates of 87.5% for Methylene Blue and 64.8% for Rhodamine B after 120 min irradiation and retained its efficiency after the fifth cycle. In another study, TiO_2@ZIF-8 revealed a porous structure with a higher surface area and photo-activity than the bare TiO_2 and SiO_2–TiO_2 [19]. Bogdan et al. produced a TiO_2/ZIF-8 photo-catalyst with different mass fractions of TiO_2 [20]. Adsorption and photocatalytic performances of these materials were evaluated to remove the model compound imidacloprid. 65% of imidacloprid adsorption was obtained after 120 min, and the 5 wt% TiO_2 loaded catalyst showed

the highest photo-activity. Cen et al. reported ZIF-8/TiO_2 for Rhodamine B degradation [21]. The composite exhibited the N–Ti–O bond formation. It also showed 95.4% degradation of the Rhodamine B within 140 min of irradiation and retained its photo-activity after recycling tests. Li et al. synthesized the ZIF-8@TiO_2 composite with a narrower band gap energy (2.98 eV) in comparison to TiO_2 (3.35 eV) and ZIF-8 (5.12 eV) [22]. The photocatalytic performance of this composite was tested for tetracycline degradation, and a 90% degradation rate was noticed after 40 min of irradiation. First-order kinetics was followed while the composite maintained its degradation ability after five cycles. Zhong et al. examined Methylene Blue and Rhodamine B degradations in the presence of TiO_2/ZIF-8 [23]. The degradation rates of these probe molecules reached approximately 90% after 40 min of illumination. Fazaeli and Aliyan also synthesized TiO_2@ZIF-8 [24]. The absorption edge of this matrix was red-shifted, and its activity was investigated for the photo-decolorization of Bromothymol Blue under UV irradiation.

In continuation of recently reported catalysts [25, 26], herein, a type 2 heterojunction hybrid frame composed of TiO_2 and ZIF-8 through a facile in situ synthesis is examined. Although there are studies in the literature about TiO_2-ZIF-8 composites, there seems to be a lack of comprehensive discussion about their potential adsorption abilities and photoactivities. The motivation of this work is three fold: the first is to improve adsorption capability and photoactivity of TiO_2 with the formation of a mesoporous TiO_2@ZIF-8 hybrid, the second is to test this material under dark and irradiation conditions via altered interactions of MO and MB and the third is to control the effect of different relative humidity conditions (40% RH, 67% RH and 84% RH) on the structure and the activity of the TiO_2@ZIF-8 hybrid. Thus, the novelty of this work lies in estimating, for the first time according to the reviewed literature, the feasibility of TıO_2–ZIF-8 hybrid and its humidified forms as type 2 heterojunctions for being potential adsorbents and photocatalysts. In line, the collaboration of ZIF-8 and TiO_2 is elaborated with several analytical techniques. The water vapor adsorption as a function of relative humidity on the TiO_2@ZIF-8 creates varying attractions for MO and MB, improving the hybrid's adsorption ability and photoactivity. As type 2 heterojunctions, all hybrids synthesized in this study are demonstrated as prospective materials for adsorption and photocatalytic processes in humidified and un-humidified environments.

2 Experimental section

2.1 Materials

Zeolitic imidazole framework (ZIF-8) is purchased from Sigma-Aldrich. Titanium tetraisopropoxide (98%, Aldrich), acetic acid (96%, Merck), 4-[[(4-dimethylamino)phenyl]-azo]benzenesulfonic acid sodium salt (Methyl Orange, Merck) and 3,7-Bis(dimethylamino)phenothiazinium chloride (Methylene Blue, Merck) are used as received without further purification. Deionized water (18MΩ-cm) is used for all experiments.

2.2 Preparation of hybrids and their humidified forms

A sol–gel method is applied for TiO_2 synthesis using titanium tetra-iso-propoxide ($Ti(OC_3H_7)_4$) and acetic acid (CH_3COOH) [27]. 20 mL of titanium tetraisopropoxide is slowly added to 80 wt% acetic acid solution at 50 °C for about 2 h. Then, the titania-sol (25% mass ratio of TiO_2 to ZIF-8) is gradually added into the ZIF-8 solution (2 g in 100 mL of water). The suspension is vigorously mixed at room temperature for 12 h and centrifuged at 6000 rpm. Thereafter, the obtained precipitate is washed extensively with deionized water. After drying at 100 °C for 12 h, the hybrid is calcined to 300 °C for 6 h and named TiO_2@ZIF-8. 25% TiO_2 is also prepared in the absence of ZIF-8 and named as TiO_2.

Humidified hybrids are prepared in a climate chamber (KKS 115 TOP + INOX/G). Before water vapor adsorption, the TiO_2@ZIF-8 hybrid is dried, and the baseline constancy is achieved. Then, it is subjected to relative humidity (RH) values of 40%, 67%, and 84% for 72 h and named TiO_2@ZIF-8 (40% RH), TiO_2@ZIF-8 (67% RH), and TiO_2@ZIF-8 (84% RH). The water vapor uptake percentages are calculated as 18%, 31%, and 42% for TiO_2@ZIF-8 (40% RH), TiO_2@ZIF-8 (67% RH), and TiO_2@ZIF-8 (84% RH), respectively. Accordingly, the percent variations between TiO_2@ZIF-8 (84% RH) and TiO_2@ZIF-8 (67% RH) are less than that between TiO_2@ZIF-8 (67% RH) and TiO_2@ZIF-8 (40% RH). This points out that TiO_2@ZIF-8 (84% RH) attains a saturation level, and is used in the detailed analysis of dark and photo-activity experiments.

2.3 Characterization

X-Ray diffraction (XRD) analysis is done in the angle range of 0–70° (2θ) using a Rigaku-D/MAX Ultima X-ray diffractometer with Cu Kα radiation ($\lambda = 1.54$ Å). Scanning electron microscopy images with EDX analysis are obtained using an ESEM-FEG/EDAX Philips XL-30 instrument operating at 20 kV. Nitrogen sorption isotherms are recorded using Quantachrome Nova 2200e. Brunauer–Emmet–Teller (BET) and BJH methods are followed for surface area and pore size measurements, respectively. Before measurements, degassing process is applied at 200 °C. A UV–vis spectrophotometer (UV-2450, Shimadzu) is used for UV–vis absorption analysis. An integrating sphere is utilized to

determine the diffuse reflectance data, with $BaSO_4$ reference. The surface electronic structure of the TiO_2@ZIF-8 hybrid is recorded via X-ray photoelectron spectroscopy (XPS) using a hemispherical electron analyzer with an Al–K micro-focused monochromator (Thermo Scientific). Calibration is performed according to the C1s line (284.6 eV).

2.4 Photocatalytic tests

A laboratory-assembled chamber is used for all experiments (Fig. 1). Reaction set-up inside the chamber utilizes a Pyrex Erlenmeyer flask as a reactor, eight black light lamps (Philips TL 15W/ 5BLB) with $\lambda_{max} = 365$ nm as irradiation sources, a cooling fan at the back of the chamber to prevent thermal effects of the lamps, and a stirrer to provide continuous mixing of the catalyst particles. The lamps are mounted on the right- and the left-hand side of the chamber to ensure uniform illumination. The photon flux is quantified as 4.7×10^{15} photons per second using potassium ferrioxalate actinometry. The reactor has an inlet from which air circulation is executed by a peristaltic pump and an outlet to collect the aliquots.

In many adsorption or photocatalytic degradation studies, dye concentrations in the range of 1–50 mg L^{-1} are commonly used [28, 29]. Thus, in a typical experiment, 0.2 g of hybrid is added to 200 mL of 3.27 mg L^{-1} MO or MB solution (unless the control of variation in the initial concentrations on the photoactivity). The selected concentration value of 3.27 mg L^{-1} is enough to allow clear monitoring of adsorption or degradation over time. Before illumination, the mixture is continuously stirred for 30 min in the dark to satisfy an adsorption–desorption equilibrium. Afterward, the suspension is irradiated for about 100 min and the hybrids are filtered through a 0.45 µm Millipore filter at certain intervals. The residual amounts of MO and MB in suspensions are measured by the decrements in the absorbance values at 464 nm and 665 nm, respectively. The same experimental set-up under similar reaction conditions is used for the dark experiments. The photocatalytic degradation percentages of MO and MB in the presence of TiO_2@ZIF-8 and humidified hybrids are higher than their adsorption percentages in the dark, indicating the photocatalytic roles of the as-prepared structures (Figs. 7c and 9d).

To check the reusability of TiO_2@ZIF-8 and TiO_2@ZIF-8 (84% RH) for repetitive four cycles, the photocatalytic experiments are repeated with the same used hybrids. After each cycle, the hybrids are centrifuged, washed with water, dried for 3 h at 70℃ and weighed. At the end of fourth cycle, TiO_2@ZIF-8 and TiO_2@ZIF-8 (84% RH) are weighed as 0.1987 g and 0.1978 g, respectively. Hence, the weight loss detected for TiO_2@ZIF-8 and TiO_2@ZIF-8 (84% RH) are calculated as 0.65% and 1.1%, respectively, pointing out negligible hybrid losses during separation and washing steps.

3 Results and discussion

3.1 Characterization studies

3.1.1 XRD analysis

XRD patterns of ZIF-8, TiO_2, and the hybrids are illustrated in Fig. 2. Anatase is noticed as the main phase of TiO_2 with diffraction peaks at 25.36°, 38.1°, 47.86°, 53.96°, 55.86°, and 62.74° (2θ), corresponding to the (101), (004), (200), (105), and (211) planes, respectively (MDI-JADE6). The typical reflections of ZIF-8 show (011), (002), (112), and (222) planes at 7.5°, 10.4°, 12.7°, and 18.4° (2θ), respectively [30, 31]. For TiO_2@ZIF-8 hybrid, TiO_2 presence is evidenced by the observation of all anatase diffractions [32]. The absence of ZIF-8 signals below 20°(2θ) indicates

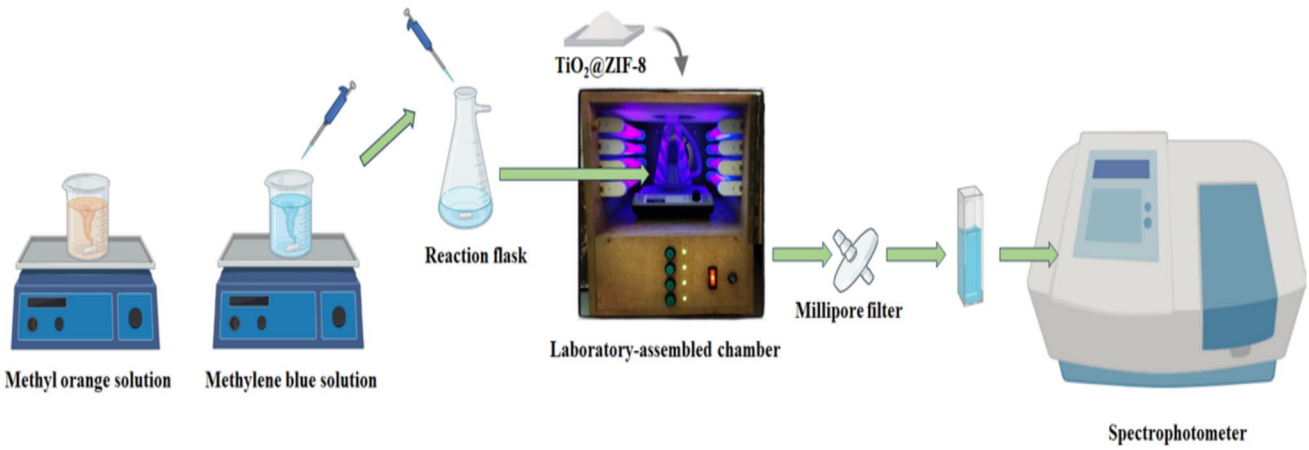


Fig. 1 Schematic steps of photocatalytic tests

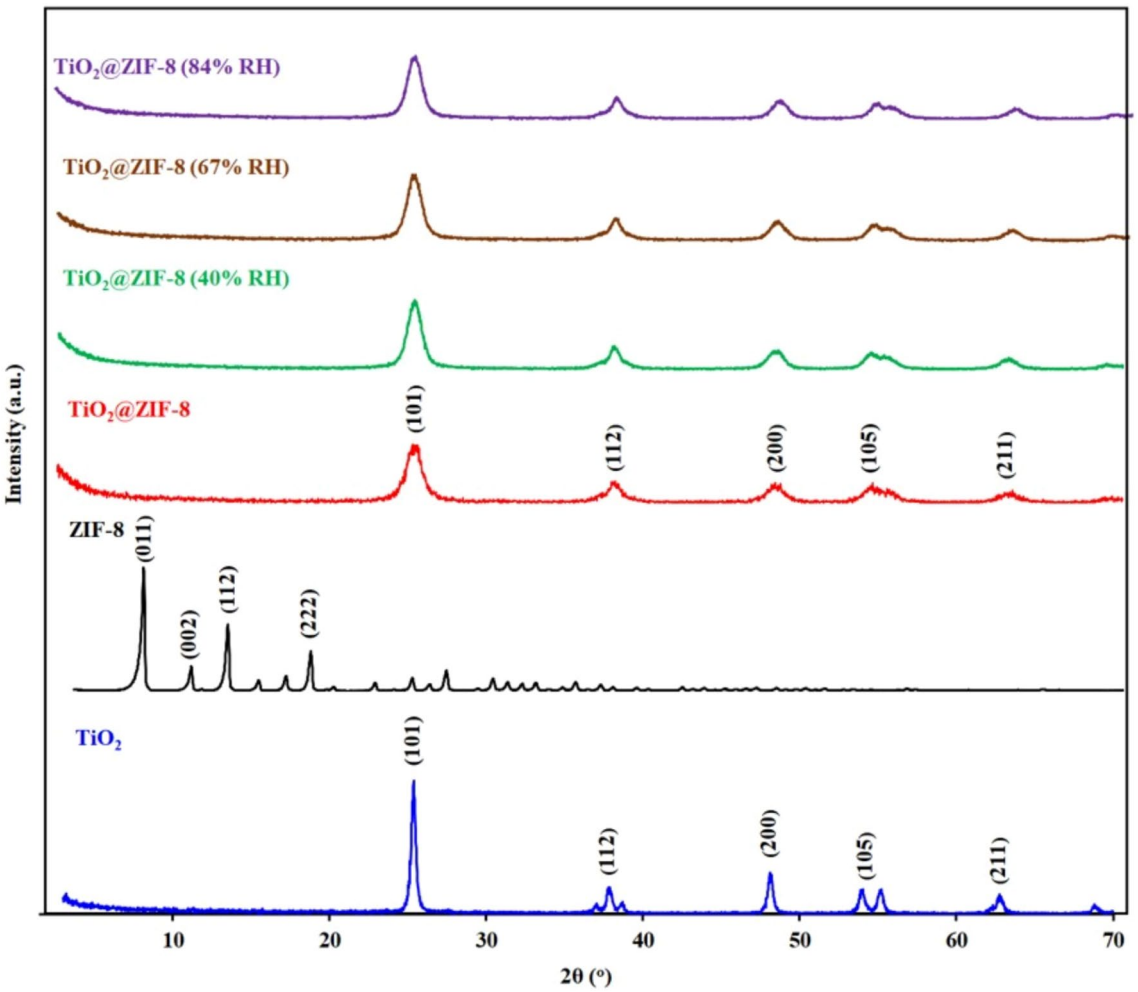


Fig. 2 XRD patterns of ZIF-8, TiO_2 and hybrids

dominance and even distribution of TiO_2 nanoparticles on the ZIF-8 matrix, which was also noticed in the study of Pi et al. [33]. Similar to TiO_2-ZIF-8, humidified hybrids demonstrate only TiO_2 peaks. Besides, humidity percentage does not alter peak positions and intensities. Crystalline sizes of TiO_2 nanoparticles are calculated from the significant (101) reflection using Scherrer's equation as 16.2 nm for TiO_2, 10.8 nm for TiO_2@ZIF-8, and 10.7–10.5 nm for humidified hybrids. Thus, the ZIF-8 frame inhibits the growth of TiO_2 aggregates and reduces their sizes within the hybrids.

3.1.2 N_2 adsorption/desorption measurements

Nitrogen sorption measurements and pore size distributions of ZIF-8, TiO_2, and TiO_2@ZIF-8 hybrid are displayed in Fig. 3. ZIF-8 demonstrates a type I isotherm, while TiO_2 reveals a type 4 isotherm with multilayer adsorptions at high pressures. For the TiO_2@ZIF-8 hybrid, porosity increases, and a type 4 isotherm is detected. Decrement in the surface area of TiO_2@ZIF-8 hybrid (135.6 $m^2\ g^{-1}$) relative to that of ZIF-8 (1288.8 $m^2\ g^{-1}$) may indicate the adsorption of TiO_2 nanoparticles on the ZIF-8 frame [26]. Meanwhile, TiO_2@ZIF-8 hybrid has a higher surface area (135.6 $m^2\ g^{-1}$) and pore volume (0.223 $cm^3\ g^{-1}$) in comparison to TiO_2 (40.1 $m^2\ g^{-1}$ and 0.001 $cm^3\ g^{-1}$). Thus, the existence of ZIF-8 within the hybrid matrix increases both surface area and the pore volume, which eventually promotes the hybrids' performance in adsorption and photo-catalysis as discussed in Sects.3.2 and 3.4.

3.1.3 UV–vis DRS analysis

Figure 4a shows the UV–vis DRS of ZIF-8, TiO_2, and the hybrids. ZIF-8 has an absorption edge (230 nm) and a long tail, while TiO_2@ZIF-8 and humidified hybrids exhibit a band (200–390 nm) analogous to TiO_2. Optical band gaps

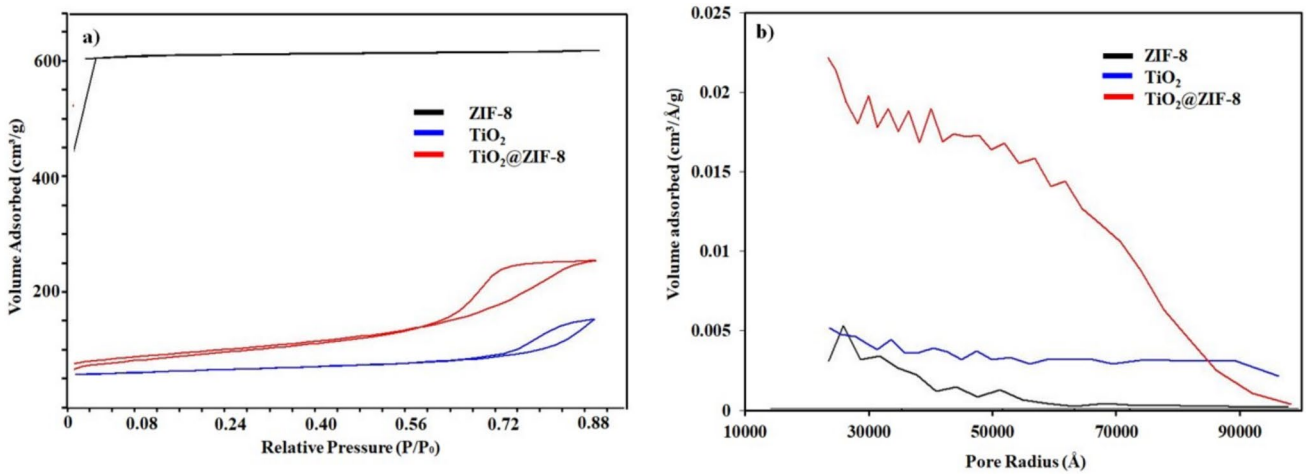


Fig. 3 **a)** Nitrogen adsorption/desorption isotherms and **b)** pore size distribution plots of ZIF-8, TiO_2, and TiO_2@ZIF-8 hybrid

are attained by transforming the results obtained from UV–vis DRS using Tauc's equation.

$$(\alpha hg)^2 = A\ (h\gamma - E_g) \quad (1)$$

where α, h, γ, E_g, and A stand for absorption extinction coefficient, Planck's constant, frequency of the light, band gap energy, and proportionality constant, respectively [34, 35]. Straight line ranges of '$(\alpha h\ \gamma)^2$ versus h γ ' plots are extended on the energy (h γ) axis to obtain band gap energies. Accordingly, E_g values are estimated as 4.9 eV for ZIF-8, 3.08 eV for TiO_2, 3.00 eV for TiO@ZIF-8, 2.95 eV for TiO_2@ZIF-8(40% RH), 2.93 eV for TiO_2@ZIF-8(67% RH), and 2.91 eV for TiO_2@ZIF-8(84% RH) (Fig. 4b, inset).

3.1.4 SEM–EDX and mapping analysis

The SEM image of ZIF-8 shows irregular square polyhedral with smooth surfaces and C (55.3 wt%), N (15.3 wt%), O (1.82 wt%), and Zn (27.6 wt%) major elements (Fig. 5a). The as-prepared TiO_2 consists of nanospheres with Ti (67.2 wt%) and O (32.8 wt%) (Fig. 5b). TiO_2@ZIF-8 maintains ZIF-8's profile while heterogeneity increases (Fig. 5c). According to the surface scan of the hybrid, it is observed that TiO_2 nanoparticles are grown on the ZIF-8's surface. This is verified with the detection of the Ti signal in the EDX analysis (Fig. 5d) and also in the mapping images where the purple, brown, green, cyan, and gray colors represent the distributions of C, N, O, Zn, and Ti, respectively (Fig. 5e–i). A magnified image of TiO_2@ZIF-8 reveals blunt edges and rough surfaces of ZIF-8's polyhedra with similar elemental compositions noticed in Fig. 5d (Fig. 5j, k). Through mapping diagrams,

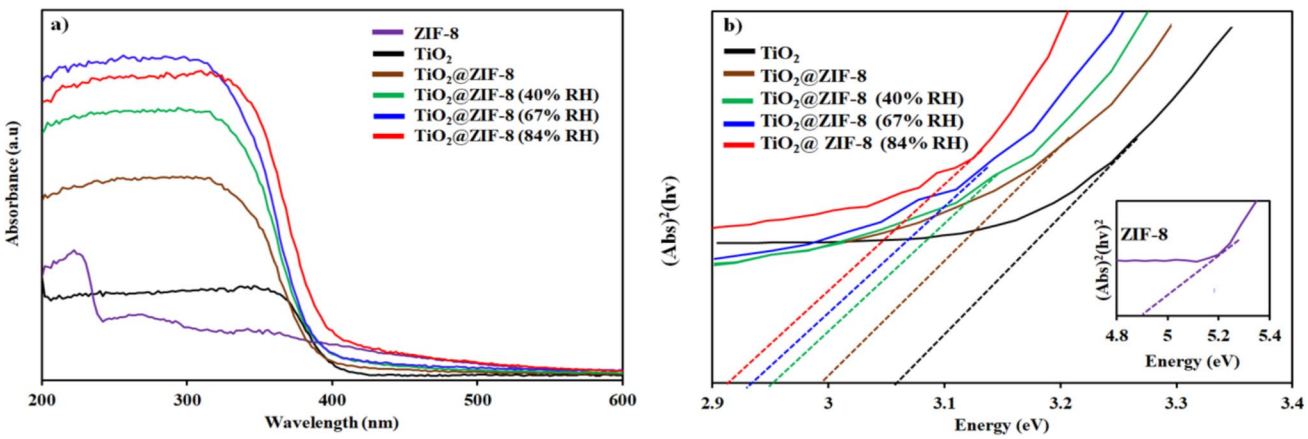


Fig. 4 **a)** UV–vis DRS spectra and **b)** band gap absorption plots of ZIF-8, TiO_2, and the hybrids

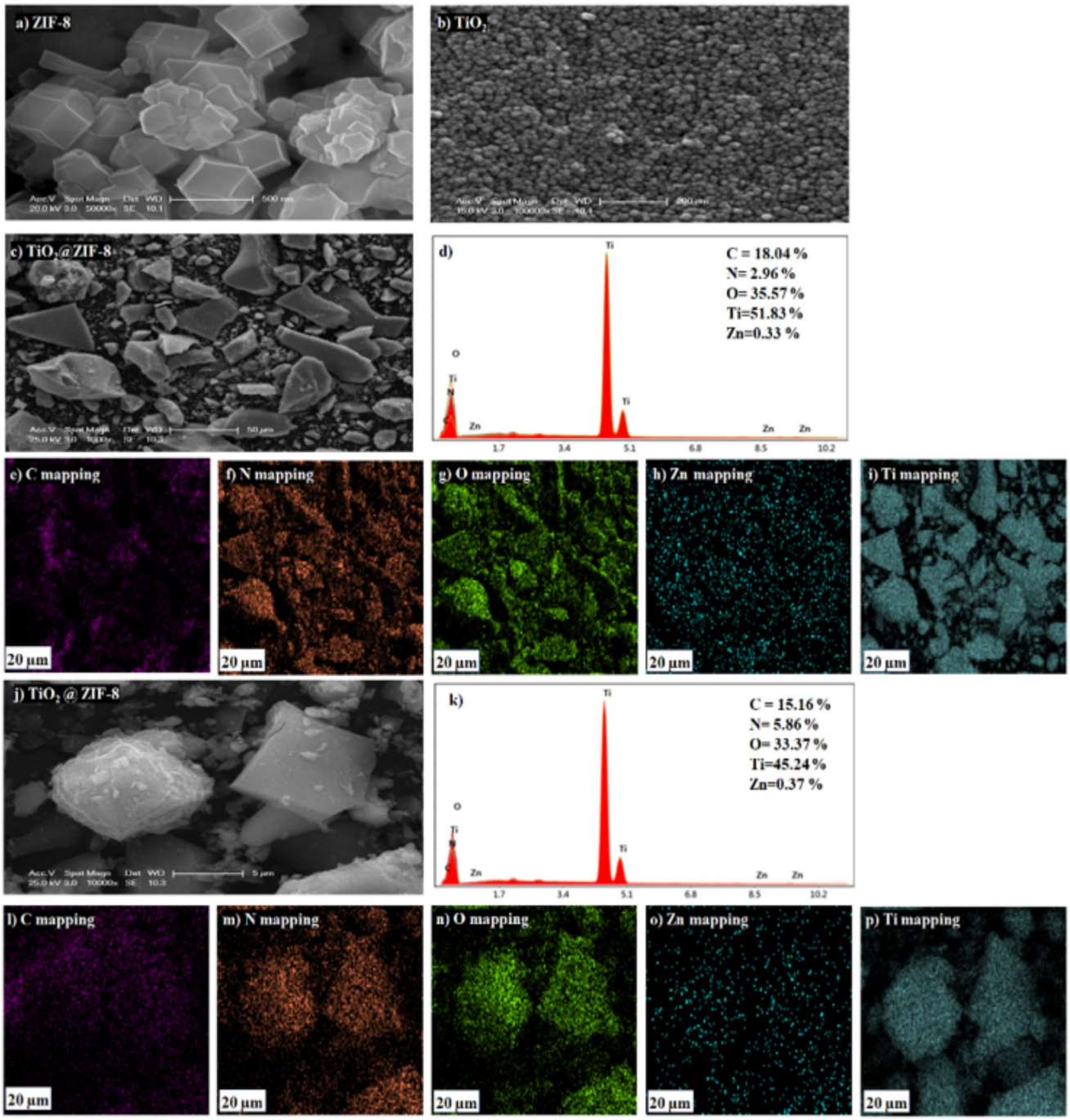


Fig. 5 SEM images of **a)** ZIF-8, **b)** TiO_2, **c**, **j)** TiO_2@ZIF-8 hybrid, **d**, **k)** EDX analysis of TiO_2@ZIF-8 hybrids, **e**–**j** and **l**–**p)** Elemental mapping analysis of TiO_2@ZIF-8 hybrids

the occurrence of Ti and O elements on the hybrids' surface again indicates TiO_2 nanoparticles' dispersion on the ZIF-8 (Fig. 5l–p).

Consequently, for TiO_2@ZIF-8, recognition of the Ti signal, increment in O percentage, and decrement in the C, N, and Zn percentages are notable relative to those in ZIF-8. Hence, TiO_2 nanoparticles loaded on the ZIF-8 matrix are expected to improve adsorption capacities and photocatalytic performances.

3.1.5 XPS analysis

Zn, O, C, N, and Ti exist as major elements of the TiO_2@ZIF-8 hybrid (Fig. 6a). Zn $2p_{3/2}$ and Zn $2p_{1/2}$ peaks are

detected at 1021.36 eV and 1044.52 eV, respectively (Fig. 6b) [36]. For ZIF-8, these energies were reported as 1020.94 eV (Zn $2p_{3/2}$) and 1044.12 eV (Zn $2p_{1/2}$) [26]. Higher binding energies of Zn 2p peaks in TiO_2@ZIF-8 hybrid relative to those of ZIF-8 indicate decrement in the electron density of ZIF-8's ligand groups. This illustrates probable electron transfer from imidazole linkers to TiO_2 as explored in the former studies [20, 21].

The O 1 s spectrum shows two peaks: the first peak belongs to the Ti–O bond at 529.65 eV, confirming the in situ growth of TiO_2 nanoparticles (Fig. 6c). The other peak is attributed to Zn–OH at 531.26 eV, which was also detected in the study of Angela et al. [37]. The C 1 s spectrum has three peaks: the peak at 284.65 eV is assigned to C–C, the one at 286.21 eV is labeled for C–N, and the last peak is attributed to C = C coordination in 2-methylimidazole structure at 288.77 eV (Fig. 6d). Two peaks are noticed in N 1 s spectrum (Fig. 6e). N–Ti–O bond formation is evidenced by the peak at 399.71 eV, implying the replacement of some O atoms of TiO_2@ZIF-8 by the N atoms of the imidazole linkers [22, 38, 39]. Such coordination simultaneously ensures the formation of the TiO_2@ZIF-8 hybrid and the possible electron transfer from ZIF-8 to TiO_2. The 401.99 eV peak represents the C–N bond in imidazole linkers. The Ti 2p spectrum has two significant peaks at 458.29 eV (for Ti $2p_{3/2}$) and 463.97 eV (for Ti $2p_{1/2}$), conforming to the existence of Ti^{4+} in TiO_2@ZIF-8 (Fig. 6f) [40, 41]. The ratio of Ti $2p_{3/2}$ to Ti $2p_{1/2}$ is found as 2.01, in line with those of TiO_2-Degussa P-25 (2.0) and 25% TiO_2 (2.1) [42]. Meanwhile, Ti peaks of TiO_2@ZIF-8 are detected at lower energies than Ti peaks (458.59 eV (for Ti $2p_{3/2}$) and 464.21 eV (for Ti $2p_{1/2}$)) of 25% TiO_2 [42]. Accordingly, increment in the electron density around the Ti atoms within TiO_2@ZIF-8 corroborates the electron flow from the ZIF-8's ligand groups to the TiO_2. A typical satellite signal of titanium oxides is noticed at 471.38 eV [43].

3.2 Dark adsorption tests

Figure 7 shows the results of dark adsorption experiments. The remaining MO and MB percentages in solution in the existence of TiO_2, ZIF-8, TiO_2@ZIF-8, and humidified hybrids are revealed in Fig. 7a, b. The impact of humidity on the adsorption processes changes in the presence of MO and MB due to the differing interactions between MO (or MB) and the hybrids. Hence, the variation in the humidity percentage for the adsorption efficiencies of MO and MB after 100 min is illustrated in Fig. 7c. As a plausible interpretation of the experimental data shown in Fig. 7a, b, the proposed

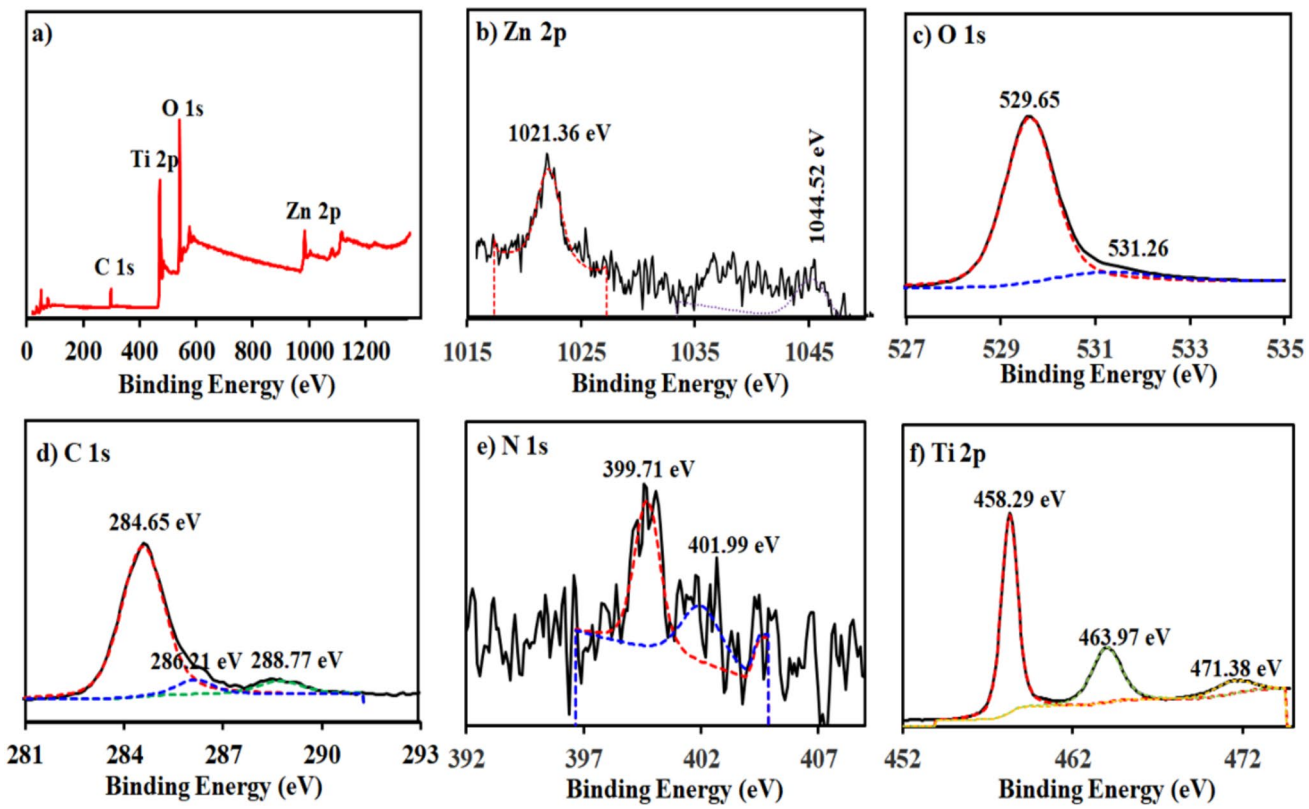


Fig. 6 **a)** Survey XPS spectrum and **b–f)** high-resolution Zn 2p, O 1 s, C 1 s, N 1 s and Ti 2p spectra of TiO_2@ZIF-8 hybrid

interactions between TiO_2@ZIF-8 hybrid (or TiO_2@ZIF-8 (84% RH) hybrid) and MO (or MB) are suggested in Fig. 7d.

The adsorption of MO on TiO_2 is limited due to the repulsive interactions between O atoms of TiO_2 and sulfonic groups of MO (Fig. 7a). ZIF-8 shows a higher adsorption ability than TiO_2 due to its large surface area and positively charged surface, attracting MO's sulfonic groups [44] (Fig. 7a). The mesoporous structure of TiO_2@ZIF-8 hybrid improves the adsorption of MO (Fig. 7a). The in situ build-up of TiO_2 nanoparticles on the ZIF-8 surface induces Lewis acid–base interactions and electrostatic attractions in addition to the already existing π–π interactions between ligand groups of ZIF-8 and MO moiety (Fig. 7d). Increment in water uptake amount from 18% for TiO_2@ZIF-8 (40% RH) to 42% for TiO_2@ZIF-8 (84% RH) decreases MO adsorption percentages owing to the repellent interactions among sulfonic groups of MO and water molecules (Fig. 7c, d).

In contrast to MO, MB's C–S + =C group may interact with the O atoms of TiO_2. This contact improves MB adsorption on TiO_2 (Fig. 7b). ZIF-8 has a lower adsorption capacity for MB owing to the repellent interactions in between positively charged surface of ZIF-8 and MB's C–S + =C group [44] (Fig. 7b). The adsorption of MB is increased with TiO_2@ZIF-8 owing to the Lewis acid–base interactions, electrostatic attractions and π–π interactions (Fig. 7b,d). Increment in the relative humidity percentage accelerates the MB's adsorption (Fig. 7c). The least MB residual percentage (24.9%) is noticed with TiO_2@ZIF-8 (84% RH) due to the establishment of hydrogen bonds between surface adsorbed water molecules on TiO_2@ZIF-8 and MB moiety (Fig. 7d).

Table 1 compares the dye adsorption ability of the TiO_2@ZIF-8 hybrid prepared in this study with the previously reported MOF-based composites. It is inferred that TiO_2@ZIF-8 hybrid's adsorption capability for MO is comparable while that for MB is better than formerly stated results.

3.3 Kinetic analysis under dark conditions

The kinetic analysis of TiO_2@ZIF-8 and TiO_2@ZIF-8 (84% RH) hybrids is also studied under dark conditions (Fig. 8a). At the beginning of the experiments, elevated adsorption rates for both MO and MB are detected. TiO_2@ZIF-8 demonstrates a higher adsorption capacity for MO than TiO_2@ZIF-8 (84% RH). Contrarily, TiO_2@ZIF-8 (84% RH) exhibits a better adsorption performance for MB adsorption than TiO_2@ZIF-8. Meanwhile, TiO_2@ZIF-8 and TiO_2@ZIF-8 (84% RH) hybrids reveal saturated adsorptions within 30 min (Fig. 8a).

To analyze these results in detail, pseudo-first- and pseudo-second-order kinetic models are evaluated (Fig. 8b, c, Table 2). For both MO and MB adsorption, the agreement between q_e(exp) and q_e(calc) values with high regression coefficients (R^2) is pronounced in the case of the pseudo-second-order model rather than the pseudo-first-order model. This may suggest an electron trade between TiO_2@ZIF-8 (or TiO_2@ZIF-8 (84% RH)) and MO (or MB) [49, 50].

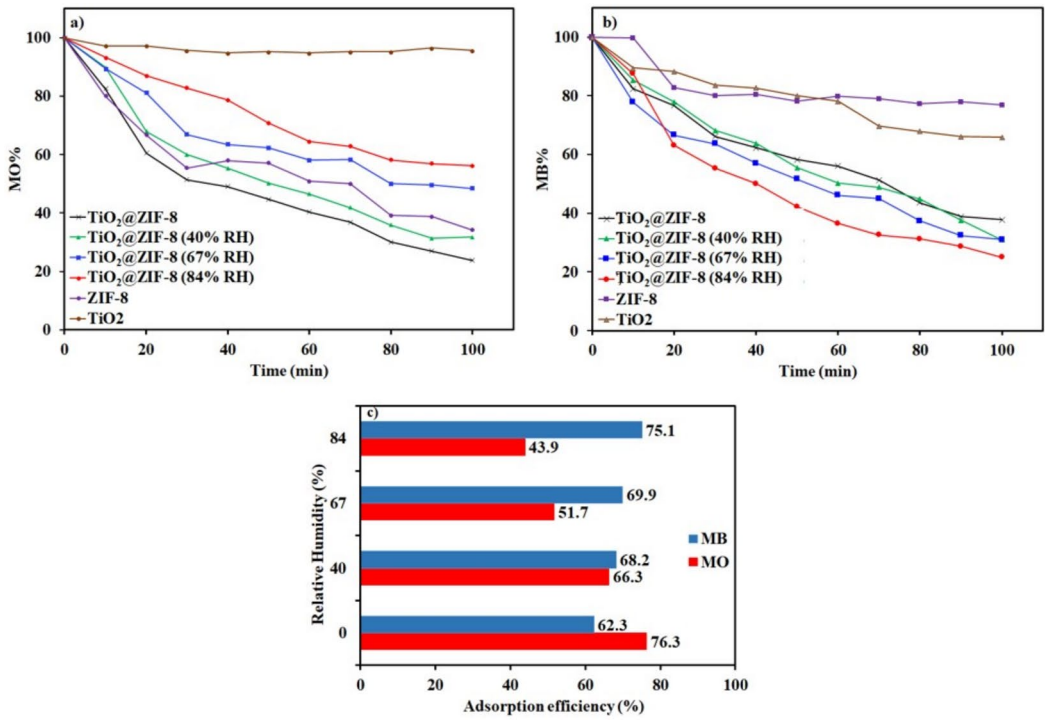
For MO, k_2 (rate constant-pseudo-second-order model) is found to be higher in the presence of TiO_2@ZIF-8 than that of TiO_2@ZIF-8 (84% RH), corroborating MO's enhanced electrostatic interactions with TiO_2@ZIF-8. On the other hand, for MB, the k_2 value is more significant in the presence of TiO_2@ZIF-8 (84% RH), confirming its better adsorption with water molecules through H bonding. Consequently, adsorption process using the TiO_2@ZIF-8 removes about 80% of MO and less MB (60%), whereas TiO_2@ZIF-8 (84% RH) use eliminates about 65% of MB and less MO (41%).

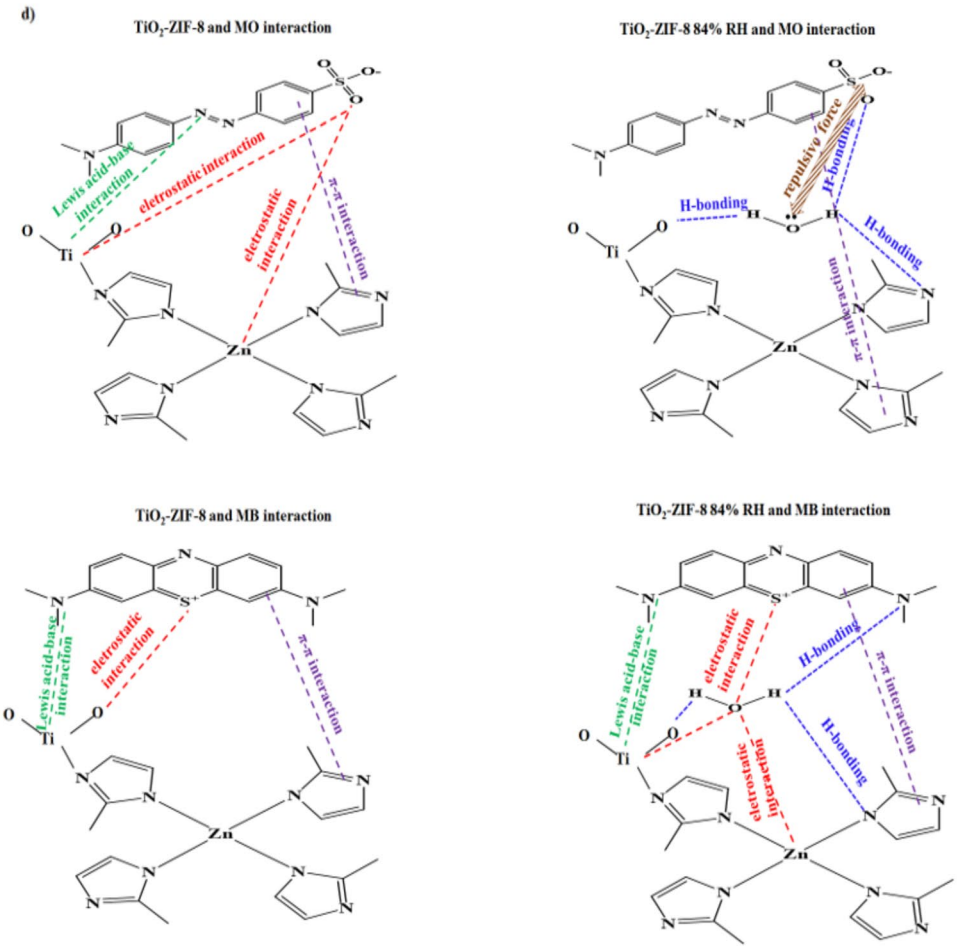
MO and MB adsorptions on TiO_2@ZIF-8 and TiO_2@ZIF-8 (84% RH) hybrids are also elucidated using Langmuir and Freundlich isotherms (Fig. 8d, e, Table 3). High correlation coefficients (R^2) obtained with Langmuir model infer that TiO_2@ZIF-8 and TiO_2@ZIF-8 (84% RH) hybrids have monolayer adsorption capacities. Besides, the adsorption of MO on TiO_2@ZIF-8 has a higher q_L value than on TiO_2@ZIF-8 (84% RH). In contrast, for MB adsorption, the q_L value is bigger with TiO_2@ZIF-8 (84% RH) than with TiO_2@ZIF-8.

3.4 Photocatalytic activities

Photolysis of MO and MB and also photo-activity of the TiO_2 are demonstrated in Fig. 9a. In the presence of ZIF-8, TiO_2@ZIF-8, and humidified hybrids, the remaining MO and MB percentages in solution are shown in Fig. 9b, c. The effect of variation in the humidity percentage for the degradation efficiencies of MO and MB after 100 min is illustrated in Fig. 9d.

The results of photolysis runs are found to be negligible, while TiO_2 existence speeds up the degradation of both MO and MB with 78% and 79% remaining percentages after 100 min irradiation, respectively (Fig. 9a). ZIF-8, TiO_2@ZIF-8, and humidified hybrids reveal significant decrement in the remaining MO percentages (Fig. 9b). During irradiation, ZIF-8 enables electron transfer from ligand amines to empty Zn orbitals, known as the ligand-to-metal charge transfer mechanism [17, 51, 52]. Then, photo-generated electrons react with water molecules in the reaction media, promote generation of hydroxyl radicals and their reactions with MO for the degradation process. For MB, degradation is found to be lower than MO in the presence of ZIF-8 due to the limited adsorption ability of ZIF-8 for MB (Fig. 9c). TiO_2@ZIF-8 improves degradations of MO and MB since their adsorptions are enriched by the existence of TiO_2 photo-catalyst nanoparticles on the ZIF-8 frame via Lewis acid–base interactions and electrostatic attractions. The success of humidified hybrids in


a)
MO%
Time (min)
TiO2@ZIF-8
TiO2@ZIF-8 (40% RH)
TiO2@ZIF-8 (67% RH)
TiO2@ZIF-8 (84% RH)
ZIF-8
TiO2
b)
MB%
Time (min)
c)
Relative Humidity (%)
Adsorption efficiency (%)
MB
MO
75.1
43.9
69.9
51.7
68.2
66.3
62.3
76.3


d)
TiO2-ZIF-8 and MO interaction
TiO2-ZIF-8 84% RH and MO interaction
TiO2-ZIF-8 and MB interaction
TiO2-ZIF-8 84% RH and MB interaction
Lewis acid-base interaction
eletrostatic interaction
π-π interaction
H-bonding
repulsive force

◂**Fig. 7** **a**, **b)** Remaining MO and MB percentages under dark conditions, **c)** MO and MB adsorption percentages as a function of relative humidity after 100 min, **d)** Postulated interactions of MO and MB with TiO_2@ZIF-8 and TiO_2@ZIF-8 (84% RH) hybrids

degradation is due to more hydroxyl radicals they provide to the reaction medium by the reaction of surface-adsorbed water molecules and holes (h^+) (will be discussed in the following paragraphs in detail). The impact of humidity percentages on the degradation efficiencies is demonstrated in Fig. 9d.

Figure 10 exhibits the plausible photocatalytic degradation mechanism in the presence of the TiO_2@ZIF-8 hybrid. Since ZIF-8's band gap energy is 4.9 eV, its electron excitation is limited under UV irradiation. Contrarily, lower band gaps of the hybrids create an electric field among ZIF-8 and TiO_2 and facilitate movements of electrons to the conduction band of TiO_2 and holes to the valence band of ZIF-8 [53]. In this respect, conduction (E_{CB}) and valence band (E_{VB}) energies of ZIF-8 and TiO_2 are calculated by the following formulas (Eqs. 2, 3):

$$E_{CB} = X - E_e - 0.5\,Eg \tag{2}$$

$$E_{VB} = E_{CB} + Eg \tag{3}$$

X is the electronegativity constant (2.36 eV for ZIF-8 and 5.81 eV for TiO_2), and E_e is 4.5 eV [54]. Accordingly, the E_{CB} values are calculated as − 4.59 eV for ZIF-8 and − 0.23 eV for TiO_2. Hence, the conduction band of TiO_2 is more positive than that of ZIF-8. The valence band of ZIF-8 (+ 0.31 eV) is less positive than that of TiO_2 (+ 2.85 eV). Thus, electrons can be transferred from the ZIF-8's highest-occupied molecular orbital (HOMO) to the lowest-unoccupied molecular orbital (LUMO) during UV irradiation [55]. Since the HOMO potential of ZIF-8 is more negative than that of the TiO_2's conduction band, TiO_2 accepts the electrons from the HOMO of ZIF-8 on its conduction band (Fig. 10, dashed blue arrow) [37, 56]. This electron transfer process from ZIF-8 to TiO_2 is also confirmed by the N–Ti–O bond formation in the XPS analysis. Simultaneously, valence band holes of TiO_2 are transferred to the valence band of ZIF-8 (Fig. 10, dashed red arrow). Thus, TiO_2@ZIF-8 and TiO_2@ZIF-8 (84% RH) hybrids form type 2 heterojunctions. Then, the individual reactions of electrons with O_2 (Fig. 10, solid blue arrow) and holes with water molecules (Fig. 10, solid red arrow) are eventually responsible for the generation of hydroxyl radicals and degradation of MO and MB with the following reactions (Eqs. 4–10).

$$ZIF-8\ and TiO_2 + h\gamma \rightarrow h^+ + e^- \tag{4}$$

$$TiO_2(e^-) + O_2 \rightarrow TiO_2 + O_2^{\cdot -} \tag{5}$$

$$ZIF-8(h^+) + H_2O/OH^- \rightarrow ZIF-8 + OH^{\cdot} \tag{6}$$

$$O_2^{\cdot -} + H^+ \rightarrow HO_2^{\cdot} \tag{7}$$

$$2HO_2^{\cdot} \rightarrow H_2O_2 + O_2 \tag{8}$$

$$H_2O_2 + e^- \rightarrow OH^- + OH^{\cdot} \tag{9}$$

$$MO\ or\ MB + OH^{\cdot} \rightarrow degradation \tag{10}$$

Meanwhile, increment in the number of hydroxyl radicals within the humid environment is strongly suggested (Eqs. 11–14). The reaction between surface-adsorbed water H_2O (ads) (as evidenced by the detection of Zn–OH peak in XPS analysis) and h^+ initiates the generation of more hydroxyl radicals in the following reactions (Eqs.11 and 14), which promote MO and MB degradation processes.

$$H_2O\ (ads) + h^+ \rightarrow OH^{\cdot} + H^+ \tag{11}$$

$$2\,OH^{\cdot} \rightarrow H_2O_2 \tag{12}$$

$$H_2O_2 + OH^{\cdot} \rightarrow O_2^{\cdot -} + H_2O + H^+ \tag{13}$$

$$H_2O_2 + O_2^{\cdot -} \rightarrow OH^{\cdot} + OH^- + O_2 \tag{14}$$

Table 1 Adsorption efficiencies of model compounds in the presence of MOF-based materials

Material	Model Compound	Dark adsorption time	Adsorption Efficiency	References
ZIF-8@TiO_2	Crystal violet	360 min	81%	[37]
Graphene-TiO_2	Crystal violet	15 min	78%	[45]
CCP@TiO_2	Congo red Methylene blue	120 min	45% 42%	[46]
MIL-101(Cr)@clay	Methyl orange	60 min	80%	[47]
TiO_2/MIL-100(Fe)	Methylene blue	60 min	48%	[48]
TiO_2@ZIF-8	Methyl orange Methylene blue	100 min	76.3% 62.3%	This study

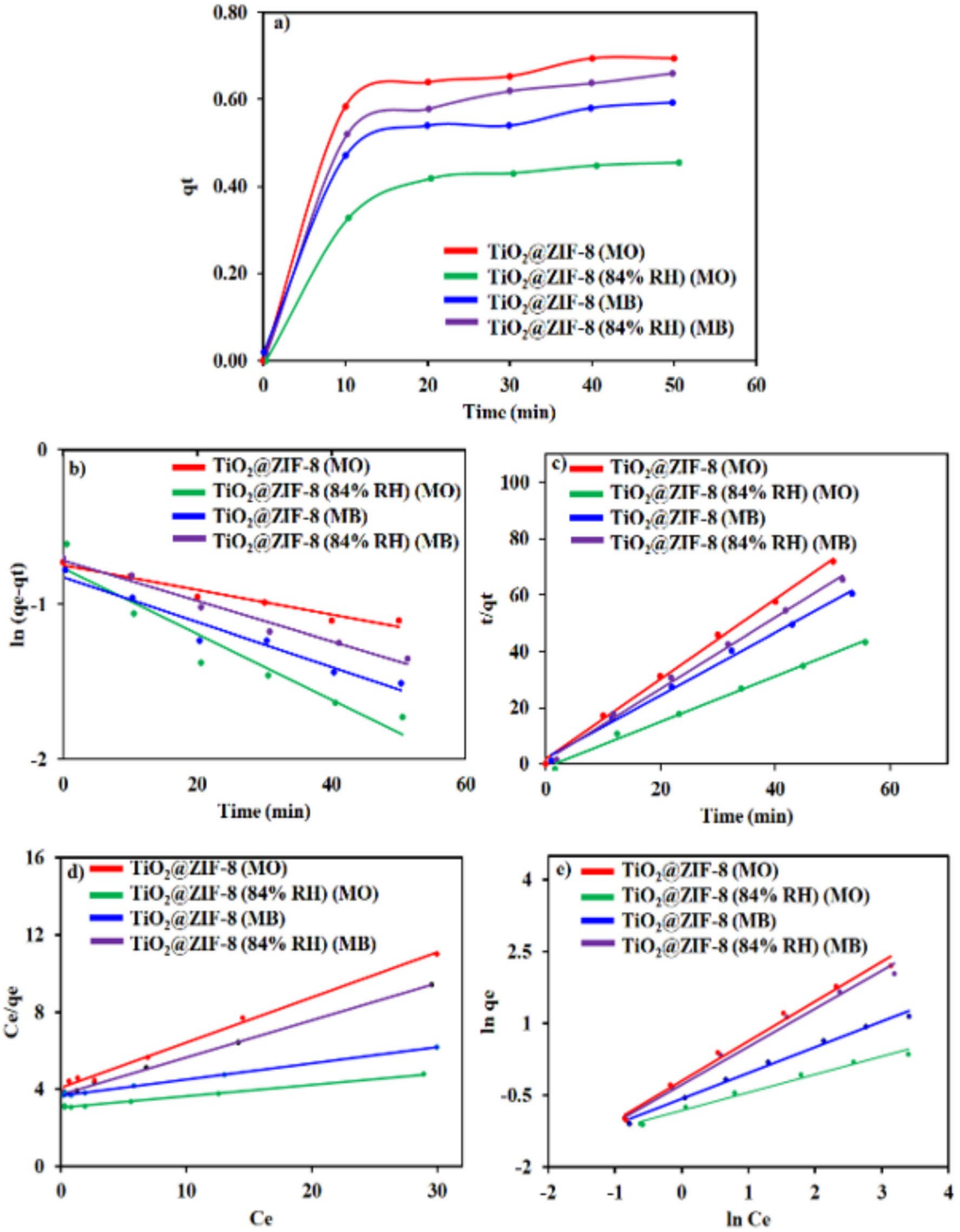


Fig. 8 **a)** Kinetic adsorption plots under dark conditions, **b**, **c)** Pseudo-first-order and pseudo-second-order kinetic analysis and **d**, **e)** Langmuir and Freundlich adsorption isotherms of TiO_2@ZIF-8 and TiO_2@ZIF-8 (84% RH) hybrids

Table 4 compares the photoactivity of the TiO_2@ZIF-8 hybrid prepared in this study with the previously reported TiO_2@ZIF-8 composites. Accordingly, TiO_2@ZIF-8 hybrid matrix can achieve higher degradation efficiency for both MO and MB within a shorter reaction period. Thus, this study discloses the collectiveness of a porous structure and a semiconductor behavior of ZIF-8 with the photocatalytic ability of TiO_2.

Table 2 Pseudo-first-order and Pseudo-second-order kinetic model parameters

		Pseudo-first order $\ln(q_e - q_t) = \ln q_e - k_1 t$ [a]			Pseudo-second order $\frac{t}{q_t} = (\frac{1}{k_2 q_e^2}) + \frac{t}{q_e}$ [a]		
	$q_{e\ (exp)}$ (mg g^{-1})	k_1 (min^{-1})	$q_{e\ (calc)}$ (mg g^{-1})	R^2	k_2 (g mg^{-1} min^{-1})	$q_{e(calc)}$ (mg g^{-1})	R^2
MO							
TiO@ZIF-8	2.310	0.008	2.110	0.977	0.918	2.390	0.997
TiO_2@ZIF-8 (84% RH)	1.980	0.005	1.720	0.940	0.798	1.990	0.994
MB							
TiO_2@ZIF-8	2.050	0.006	1.870	0.949	0.8694	2.101	0.995
TiO_2@ZIF-8(84% RH)	2.140	0.007	1.940	0.951	0.9173	2.190	0.995

[a] k_1 and k_2, pseudo-first and pseudo-second order rate constants, respectively; R^2, correlation coefficient; q_t and q_e, adsorption capacities at time "*t*" and at equilibrium, respectively

Table 3 Langmuir and Freundlich adsorption model parameters

	Langmuir $\frac{C_e}{q_e} = \frac{1}{K_L q_L} + \frac{C_e}{q_L}$			Freundlich $\ln q_e = \ln K_F + \frac{1}{n} \ln C_e$		
	K_L	q_L	R^2	K_F	1/n	R^2
MO						
TiO_2@ZIF-8	0.445	4.991	0.999	2.234	0.689	0.991
TiO_2@ZIF-8 (84% RH)	0.332	4.031	0.993	2.010	0.587	0.986
MB						
TiO_2@ZIF-8	0.378	4.121	0.994	2.078	0.612	0.988
TiO_2@ZIF-8 (84% RH)	0.409	4.561	0.995	2.121	0.623	0.989

[a] K_L and K_F, Langmuir and Freundlich constants (L mg^{-1}), respectively; q_e, and q_L, adsorption capacity at equilibrium point and maximum adsorption capacity (mg g^{-1}), respectively; C_e, equilibrium concentration (mg L^{-1}); 1/n, heterogeneity factor

3.5 Kinetic analysis under irradiation

The variation in the initial MO and the initial MB concentrations on the photoactivities of TiO_2@ZIF-8 and TiO_2@ZIF-8 (84% RH) is examined in Fig. 11a-d. The first-order reaction rates of the hybrids are explored using Eq. 14:

$$\ln\left([\mathrm{dye}]_0 / [\mathrm{dye}]_t\right) = -k\,t \tag{14}$$

where $[dye]_0$ refers to MO or MB initial concentration after the dark adsorption, $[dye]_t$ represents the residual concentration of MO or MB at time "*t*", and '*k*' stands for the rate constant. First-order kinetics elucidate high regression values with rate constants (calculated from the slopes) of 0.0129 min^{-1}, 0.0134 min^{-1}, 0.0112 min^{-1}, and 0.0146 min^{-1} for TiO_2@ZIF-8 (MO), TiO_2@ZIF-8 (84% RH) (MO), TiO_2@ZIF-8 (MB), and TiO_2@ZIF-8 (84% RH) (MB), respectively (Fig. 8e). Accordingly, TiO_2@ZIF-8 (84% RH) has higher '*k*' values for both MO and MB relative to that of TiO_2@ZIF-8. This ensures that the number of $OH^{\bullet}$ radicals is accelerated in a humid environment, being responsible for improved photoactivity.

The Langmuir–Hinshelwood model also describes the kinetic analysis of TiO_2@ZIF-8 and TiO_2@ZIF-8 (84% RH) hybrids using Eq. 15 and its linearized form (Eq. 16).

$$Rate = \frac{kK([dye]_0}{1 + K[dye]_0} \tag{15}$$

$$\frac{1}{Rate} = \frac{1}{kK[dye]_0} + \frac{1}{k} \tag{16}$$

Accordingly, the line intercept determines the reaction rate constant (*k*), and the slope gives the adsorption coefficient (*K*). The results of the Langmuir–Hinshelwood kinetic analysis are summarized in Table 5 and Fig. 8f–g, where TiO_2@ZIF-8 (84% RH) shows the highest *K* and *k* values for both MO and MB.

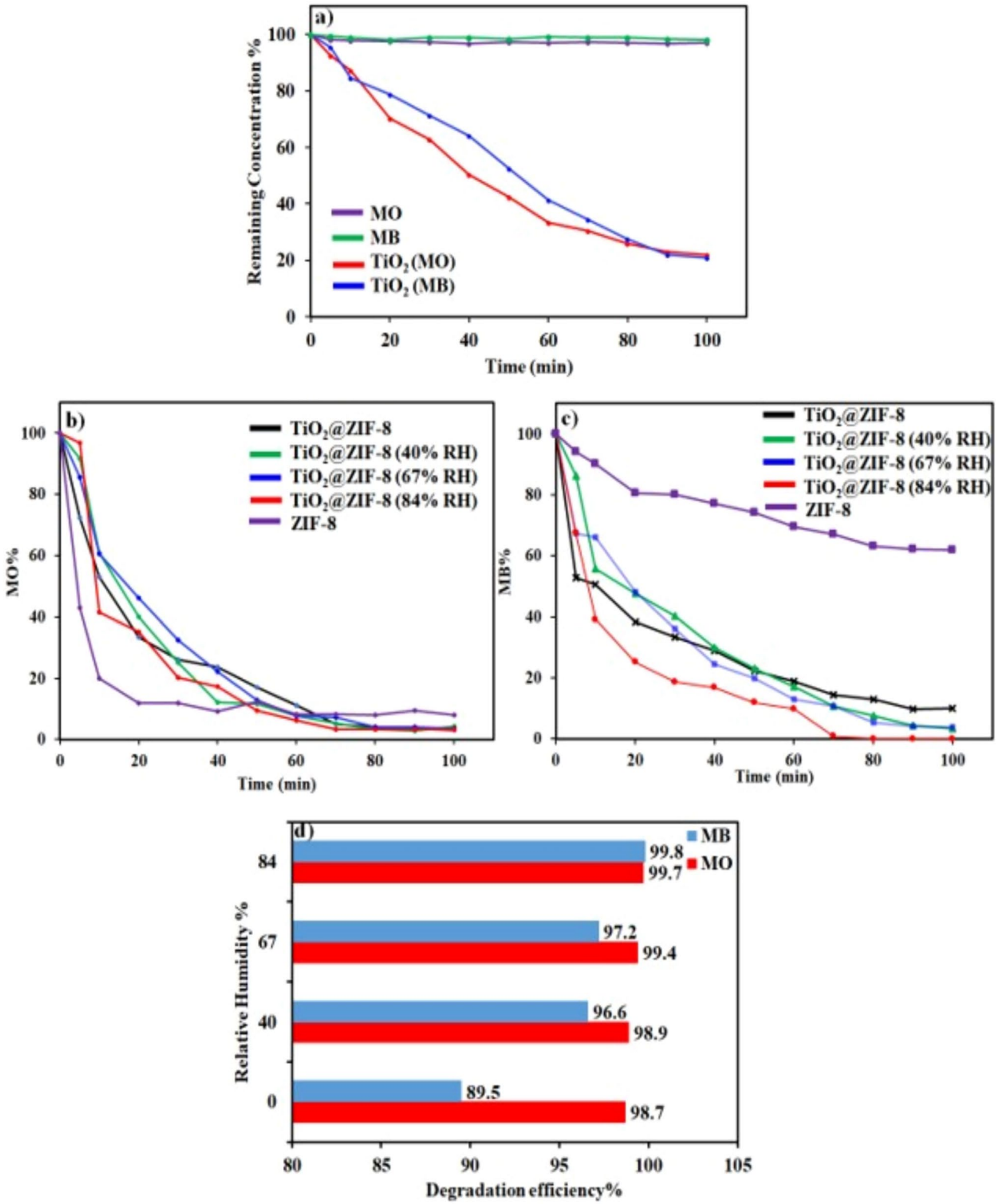


Fig. 9 **a)** Results of control experiments, **b**, **c)** Photocatalytic performances of ZIF-8, TiO_2@ZIF-8, and humidified hybrids, **d)** MO and MB degradation percentages as a function of relative humidity after 100 min irradiation

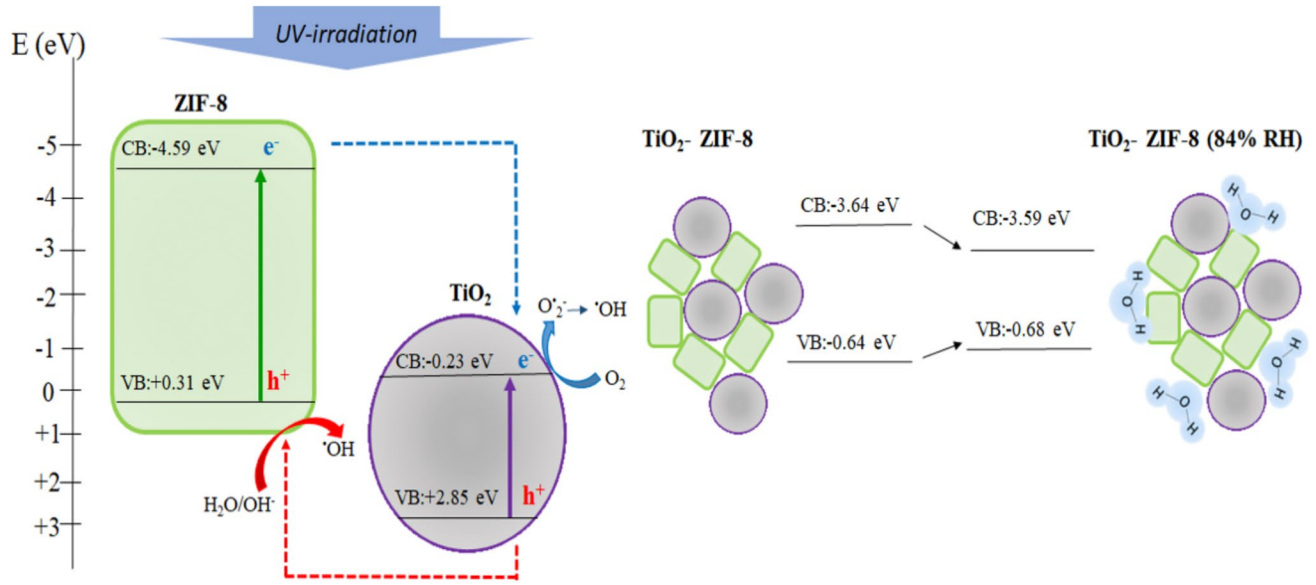


Fig. 10 Postulated carrier transfer mechanism of TiO_2@ZIF-8 and TiO_2@ZIF-8 (84% RH) hybrids under UV irradiation

Table 4 Photocatalytic degradation of model compounds in the presence of TiO_2@ZIF-8

Photocatalyst	Model Compound	Light source	Irradiation Time	Efficiency	References
TiO_2@ZIF-8	Methylene Blue	UV	180 min	99.1%	[15]
TiO_2/ZIF-8	Methylene Blue	Visible	24 min	93.36%	[19]
TiO_2@ZIF-8	Methylene Blue and Rhodamine B	UV	120 min	87.5% and 64.8%	[14]
ZIF-8@TiO_2	Crystal violet	UV	1080 min	92.3%	[29]
ZIF-8/TiO_2	Rhodamine B	UV	4 h	95.4%	[17]
TiO_2/ZIF-8	Tetracycline	Visible	90 min	90%	[27]
TiO_2@ZIF-8	Methyl Orange and Methylene Blue	UV	100 min	99% and 89.5%	This study

3.6 Reusability tests

The photocatalytic stability and the reusability of TiO_2@ZIF-8 and TiO_2@ZIF-8 (84% RH) hybrids are controlled throughout four cycles under irradiation (Fig. 12a). After the fourth-cycle degradation of MO or MB, slight decrement in degradation percentages and negligible weight losses is detected for TiO_2@ZIF-8 (0.65%) and TiO_2@ZIF-8 (84% RH) (1.1%). In addition, XRD profiles of TiO_2@ZIF-8 and TiO_2@ZIF-8 (84% RH) are controlled at the end of the fourth cycle. In this respect, it is noted that the phase composition and the crystallinity of the hybrids do not change since the peak locations do not shift and new diffraction peaks are not observable (Fig. 12b). As a result, TiO_2@ZIF-8 and TiO_2@ZIF-8 (84% RH) are stable and recyclable for the photocatalytic degradation of MO and MB, which are vital for their practical applications.

4 Conclusion

In this study, TiO_2@ZIF-8 hybrid as a type 2 heterojunction is successfully synthesized using a sol–gel technique. Then, humidified hybrids are prepared at different relative humidity conditions within the climate chamber. For the TiO_2@ZIF-8 hybrid, the dominance of TiO_2 peaks is observed in the XRD analysis. It also induces a mesoporous structure with a higher surface area in comparison to TiO_2. TiO_2@ZIF-8 and humidified hybrids demonstrate decrements in the band gap energies relative to those of ZIF-8 and TiO_2. Detection of the Ti signal in SEM-mapping images while maintaining ZIF-8's polyhedral profile also verifies the TiO_2 formation on the ZIF-8 surface. XPS analysis ensures the formation of the N–Ti–O bond via electron migration from the ZIF-8 to TiO_2, which eventually suppresses the encounter rate of charge carriers. Although hybrids reveal different interactions with MO and MB, they all demonstrate

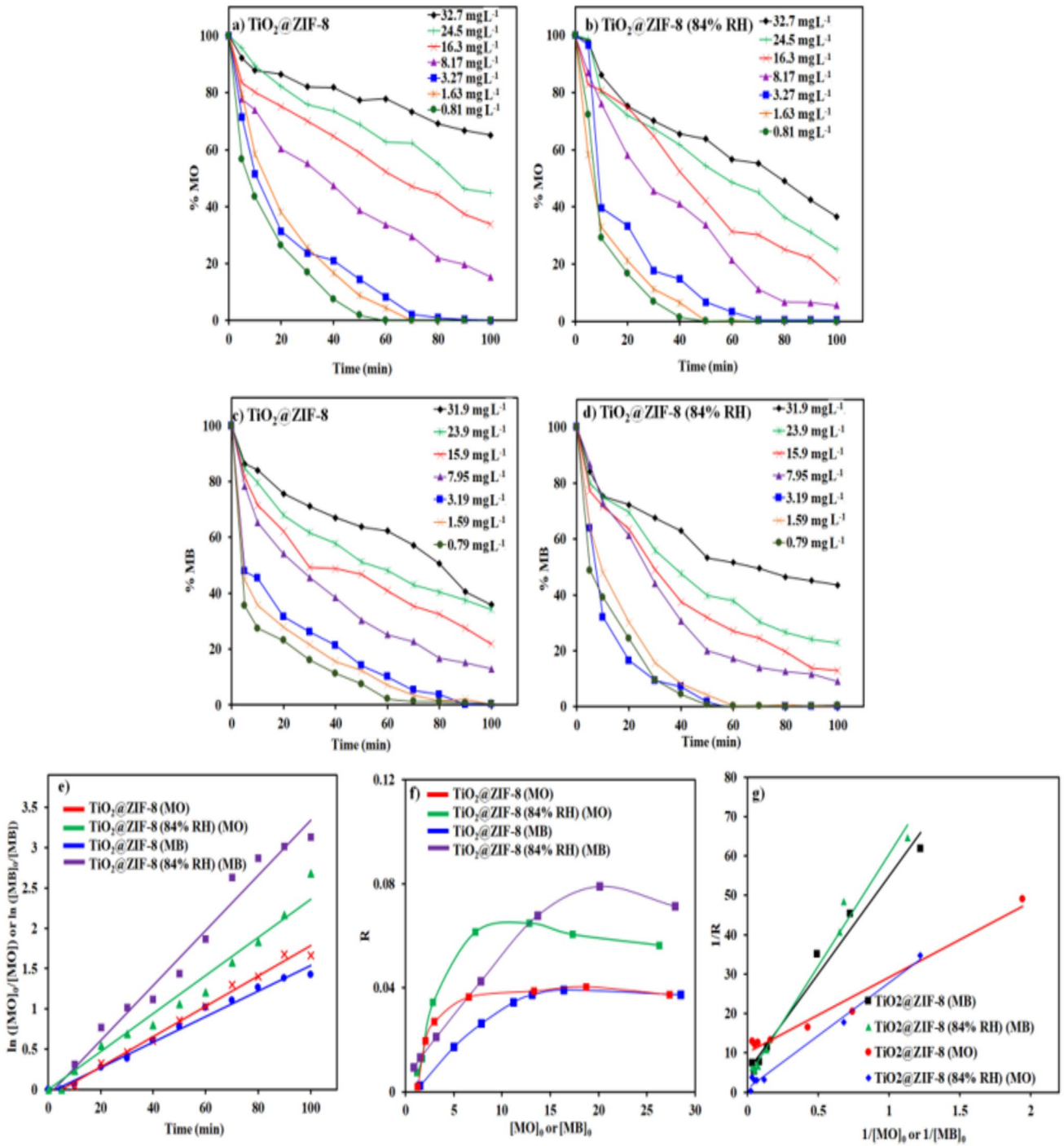


Fig. 11 Kinetic analysis: **a**–**d)** Effect of initial dye concentrations, **e)** First-order kinetic examination, **f**–**g)** Langmuir–Hinshelwood model application

Table 5 Langmuir–Hinshelwood kinetic analysis

	K (L mg^{-1})	k (mg L^{-1} min^{-1})	R^2
MO			
TiO_2@ZIF-8	0.120	0.171	0.993
TiO_2@ZIF-8 (84% RH)	0.164	0.197	0.998
MB			
TiO_2@ZIF-8	0.111	0.148	0.994
TiO_2@ZIF-8 (84% RH)	0.192	0.182	0.995

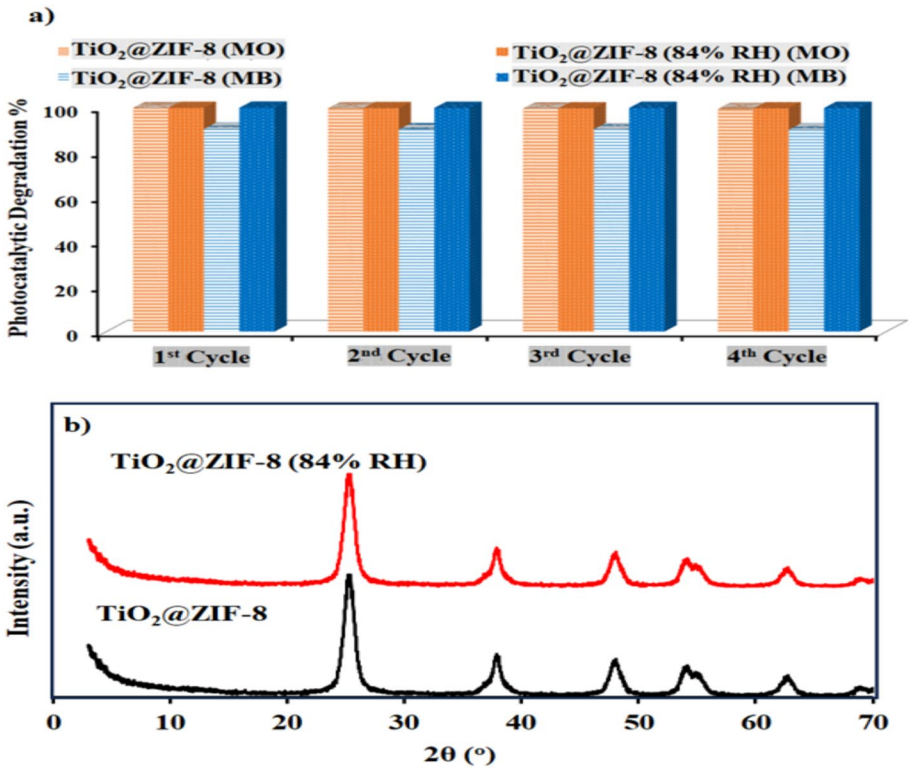


Fig. 12 **a)** Reusability tests of TiO_2@ZIF-8 and TiO_2@ZIF-8 (84% RH) hybrids and **b)** XRD patterns of TiO_2@ZIF-8 and TiO_2@ZIF-8 (84% RH) after the 4th-cycle degradations of MO or MB

excellent photoactivities under UV irradiation. Langmuir model and pseudo-second-order model align adsorption kinetics under dark conditions. The enhancement in the photoactivities of TiO_2@ZIF-8 and humidified hybrids is attributed to the accelerated electron mobility and hence promoted charge carrier separation. Photocatalytic experiments follow first-order kinetics and reveal the applicability of the Langmuir–Hinshelwood model. The reusability of TiO_2@ZIF-8 and TiO_2@ZIF-8 (84% RH) hybrids is confirmed by four consecutive cycles. These discoveries contribute significantly to the field of adsorption and photocatalysis and provide valuable insights into the type 2 heterojunction photocatalysts composed of ZIF-8 and TiO_2.

Acknowledgements This study was supported by Boğaziçi University Research Fund Grant Number-BAP 22BD8/19362.

Funding Open access funding provided by the Scientific and Technological Research Council of Türkiye (TÜBİTAK).

Declarations

Conflict of interest The authors declare that they have no known competing financial interests or personal relationships that could have appeared to influence the work reported in this paper.

Open Access This article is licensed under a Creative Commons Attribution 4.0 International License, which permits use, sharing, adaptation, distribution and reproduction in any medium or format, as long as you give appropriate credit to the original author(s) and the source, provide a link to the Creative Commons licence, and indicate if changes were made. The images or other third party material in this article are included in the article's Creative Commons licence, unless indicated otherwise in a credit line to the material. If material is not included in the article's Creative Commons licence and your intended use is not permitted by statutory regulation or exceeds the permitted use, you will need to obtain permission directly from the copyright holder. To view a copy of this licence, visit http://creativecommons.org/licenses/by/4.0/.

References

1. Tejashwini, D. M., Harini, H. V., Nagaswarupa, H. P., Naik, R., Deshmukh, V. V., & Basavaraju, N. (2023). An in-depth exploration of eco-friendly synthesis methods for metal oxide nanoparticles and their role in photocatalysis for industrial dye degradation. *Chemical Physics Impact, 7*, Article 100355. https://doi.org/10.1016/j.chphi.2023.100355
2. Heryanto, H., Tahir, D., Akmal, A., Akouibaa, A., & Rahmat, R. (2024). Photocatalysis and microwave absorption performance of cobalt particles dispersed on activated carbon surface under the role of surface, optical, and magnetic properties. *Materials Chemistry and Physics, 327*, Article 129902. https://doi.org/10.1016/j.matchemphys.2024.129902
3. Heryanto, H., Tahir, D., Abdullah, B., Setiawan, V., Partini, J., Ilyas, S., Akouibaa, A., Rinovian, A., & Merita, M. (2024). IoT real-time monitoring system implemented to observe sunlight-influenced methylene blue degradation by AC/HAp. *Environmental Science and Pollution Research, 31*, 64033–64047. https://doi.org/10.1007/s11356-024-35514-w
4. Heryanto, H. (2025). Rice husk-derived biosilica/clay hybrids for photocatalytic dye degradation. *Materials Chemistry and Physics, 332*, Article 130245. https://doi.org/10.1016/j.matchemphys.2024.130245
5. Heryanto, H., & Tahir, D. (2025). Trends, mechanisms, and the role of advanced oxidation processes in mitigating azo, triarylmethane, and anthraquinone dye pollution: A bibliometric analysis. *Inorganic Chemistry Communications, 175*, Article 114104. https://doi.org/10.1016/j.inoche.2025.114104
6. Heryanto, H., Tahir, D., Abdullah, B., Kavgaci, M., Rinovian, A., Masrour, R., Prasad, V. S. R., & Sayyed, M. I. (2024). Carbon as a multifunctional material in supporting adsorption performance for water treatment: Science mapping and review. *Desalination and Water Treatment, 320*, Article 100758. https://doi.org/10.1016/j.dwt.2024.100758
7. Schneider, J., Matsuoka, M., Takeuchi, M., Zhang, J., Horiuchi, Y., Anpo, M., & Bahnemann, D. W. (2014). Understanding TiO_2 photocatalysis: Mechanisms and materials. *Chemical Reviews, 114*, 9919–9986. https://doi.org/10.1021/cr5001892
8. Meng, A., Zhang, L., Cheng, B., & Yu, J. (2019). Dual cocatalysts in TiO_2 photocatalysis. *Advanced Materials, 1807660*, 1–3. https://doi.org/10.1002/adma.201807660
9. Sreekumar, A., Ravipati, M., & Badhulika, S. (2023). Cu-MOF nanosheets modified nickel foam: A versatile platform for highly sensitive electrochemical detection of transferrin in simulated human blood serum. *Ceramics International, 49*, 31744–31751. https://doi.org/10.1016/j.ceramint.2023.07.129
10. Yao, T., Tan, Y., Zhou, Y., Chen, Y., & Xiang, M. (2022). Preparation of core-shell MOF-5/Bi2WO6 composite for the enhanced photocatalytic degradation of pollutants. *Journal of Solid State Chemistry, 308*, Article 122882. https://doi.org/10.1016/j.jssc.2022.122882
11. Sandhu, Z. A., Farwa, U., Danish, M., Raza, M. A., Talib, A., Amjad, H., Riaz, R., & Al-Sehemi, A. G. (2024). Sustainability and photocatalytic performance of MOFs: Synthesis strategies and structural insights. *Journal of Cleaner Production, 470*, Article 143263. https://doi.org/10.1016/j.jclepro.2024.143263
12. Gautam, S., Agrawala, H., Thakura, M., Akbarib, A., Shardac, H., Kaura, R., & Amini, M. (2020). Metal oxides and metal organic frameworks for the photocatalytic degradation: A review. *Journal of Environmental Chemical Engineering, 8*(3), Article 103726. https://doi.org/10.1016/j.jece.2020.103726
13. Gui, X., Zhou, Y., Pan, D., Li, H., Wang, Y., Liang, Q., Zhou, M., & Li, Z. (2024). Construction of ternary Ni_2P/ZIF-8/CdS composite for efficient photocatalytic hydrogen production and pollutant degradation: Accelerating separation of photogenerated carriers. *Journal of Physics and Chemistry of Solids, 190*, 11983. https://doi.org/10.1016/j.jpcs.2024.111983
14. Chen, H., Wang, Y., Huang, F., Tu, C., & Cui, L. (2021). Layer by layer self-assembly MoS2/ZIF-8 composites on carboxyl cotton fabric for enhanced visible light photocatalysis and recyclability. *Applied Surface Science, 565*, Article 150458. https://doi.org/10.1016/j.apsusc.2021.150458
15. Liu, J. X., Li, R., Wang, Y. F., Wang, Y. W., Zhang, X. C., & Fan, C. M. (2017). The active roles of ZIF-8 on the enhanced visible photocatalytic activity of Ag/AgCl: Generation of superoxide radical and adsorption. *Journal of Alloys and Compounds, 693*, 543–549. https://doi.org/10.1016/j.jallcom.2016.09.201
16. Dai, H., Yuan, X., Jiang, L., Wang, H., Zhang, J., Zhang, J., & Xiong, T. (2021). Recent advances on ZIF-8 composites for adsorption and photocatalytic wastewater pollutant removal: Fabrication, applications and perspective. *Coordination Chemistry Reviews, 441*, Article 213985. https://doi.org/10.1016/j.ccr.2021.213985
17. Zeng, X., Huang, L. Q., Wang, C. N., Wang, J. S., Li, J. T., & Luo, X. T. (2016). Sonocrystallization of ZIF-8 on electrostatic spinning TiO_2 nanofibers surface with enhanced photocatalysis property through synergistic effect. *ACS Applied Materials & Interfaces, 8*(31), 20274–20282.
18. Chandra, R., Mukhopadhyay, S., & Nath, M. (2016). TiO_2@ZIF-8: A novel approach of modifying micro-environment for enhanced photo-catalytic dye degradation and high usability of TiO_2 nanoparticles. *Materials Letters, 164*, 571–574. https://doi.org/10.1016/j.matlet.2015.11.018
19. Fu, N., & Ren, X. (2020). Synthesis of Double-Shell Hollow TiO_2@ZIF-8 Nanoparticles With Enhanced Photocatalytic Activities. *Frontiers in Chemistry, 8*, Article 578847. https://doi.org/10.3389/fchem.2020.578847
20. Bogdan, L., Palcic, A., Duplancic, M., Leskovac, M., & Tomasic, V. (2023). Eco-Friendly Synthesis of TiO_2/ZIF-8 Composites: Characterization and Application for the Removal of Imidacloprid from Wastewater. *Processes, 11*, 963.
21. Cen, L., Tang, T., Yu, F., Wu, H., Li, C., Zhu, H., & Guo, Y. (2023). Fabrication of ZIF-8/TiO_2 electrospinning nanofibers for synergistic photodegradation in dyeing wastewater. *Journal of Industrial and Engineering Chemistry, 126*, 537–545. https://doi.org/10.1016/j.jiec.2023.06.042
22. Li, R., Li, W., Jin, C., He, Q., & Wang, Y. (2020). Fabrication of ZIF-8@TiO_2 micron composite via hydrothermal method with enhanced absorption and photocatalytic activities in tetracycline degradation. *Journal of Alloys and Compounds, 825*, Article 154008. https://doi.org/10.1016/j.jallcom.2020.154008
23. Zhong, W., Ma, B., Han, J., Chen, L., Jing, S. J., Zhang, G., & Lei, C. (2024). Design of TiO_2/ZIF-8 heterojunction with enhanced visible light photocatalytic activity under mild conditions. *Journal of the Chinese Chemical Society, 71*, 128–139. https://doi.org/10.1016/j.micromeso.2020.110401
24. Fazaeli, R., & Aliyan, H. (2019). Novel hierarchical TiO_2@ZIF-8 for photodecolorization of semi-real sample bromothymol blue aqueous solution. *Journal of the Iranian Chemical Society, 16*, 1–9. https://doi.org/10.1007/s13738-018-1475-z
25. Ökte, A. N., Karamanis, D., Chalkia, E., & Tuncel, D. (2017). The effect of ZnO or TiO_2 loaded nanoparticles on the adsorption and photocatalytic performance of Cu-BTC and ZIF-8 MOFs. *Materials Chemistry and Physics, 187*, 5–10. https://doi.org/10.1016/j.matchemphys.2016.11.059
26. Tuncel, D., & Ökte, A. N. (2021). Improved adsorption capacity and photoactivity of ZnO-ZIF-8 nanocomposites. *Catalysis Today, 361*, 191–197. https://doi.org/10.1016/j.cattod.2020.04.014
27. Kaneko, T., Fuji, M., Kodama, T., & Kitayama, Y. (2001). Synthesis of titania pillared mica in aqueous solution of acetic acid.

Journal of Porous Materials, 8, 99–109. https://doi.org/10.1023/A:1009634506284
28. Galindo, C., Jacques, P., & Kalt, A. (2000). Photodegradation of the aminoazobenzene acid orange 52 by three advanced oxidation processes: UV/H_2O_2, UV/TiO_2 and VIS/TiO_2: Comparative mechanistic and kinetic investigations. *Journal of Photochemistry and Photobiology, A: Chemistry, 130*, 35–47. https://doi.org/10.1016/S1010-6030(99)00199-9
29. Kader, S., Md, R., Al-Mamun, B. K., Suhan, S. B., & Shuchi, S. Islam. (2022). Enhanced photodegradation of methyl orange dye under UV irradiation using MoO3 and Ag doped TiO2 photocatalysts. *Environmental Technology & Innovation, 27*, Article 102476. https://doi.org/10.1016/j.eti.2022.102476
30. Saliba, D., Ammar, M., Rammal, M., Al-Ghoul, M., & Hmadeh, M. (2018). Crystal growth of ZIF-8, ZIF-67, and their mixed-metal derivatives. *Journal of the American Chemical Society, 140*, 1812–1823. https://doi.org/10.1021/jacs.7b11589
31. Wee, L. H., Janssens, N., Sree, S. P., Wiktor, C., Gobechiya, E., Fischer, R. A., Kirschhock, C. E. A., & Martens, J. A. (2014). Local transformation of ZIF-8 powders and coatings into ZnO nanorods for photocatalytic application. *Nanoscale, 6*, 2056–2060. https://doi.org/10.1039/C3NR05289C
32. Baamer, D. F., Helmy, E. T., Mostafa, M. M. M., & Pan, J. H. (2024). Synthesis of TiO_2 nanoparticles using different routes with enhanced photocatalytic and antibacterial properties. *Ceramics International, 50*, 15780–15789. https://doi.org/10.1016/j.ceramint.2024.02.058
33. Pi, H., Zhang, D., Zhang, X., Jin, Z., Zhang, L., Cui, X., & Zheng, W. (2018). Passivation of the surface imperfection of TiO_2 by using ZIF-8 for efficient carrier separation/transfer. *Dalton Transactions, 47*, 209–214. https://doi.org/10.1039/C7DT03972G
34. Chuaicham, C., Pawar, R., & Sasaki, K. (2019). Dye-sensitized photocatalyst of sepiolite for organic dye degradation. *Catalysts, 9*, 235. https://doi.org/10.3390/catal9030235
35. Chuaicham, C., Karthikeyan, S., Song, J. T., Ishihara, T., Ohtani, B., & Sasaki, K. (2020). Importance of $ZnTiO_3$ phase in ZnTi-mixed metal oxide photocatalysts derived from layered double hydroxide. *ACS Applied Materials & Interfaces, 12*, 9169–9180. https://doi.org/10.1021/acsami.9b18785
36. Tian, F., Cerro, A. M., Mosier, A. M., Wayment-Steele, H. K., Shine, R. S., Park, A., Webster, E. R., Johnson, L. E., Johal, M. S., & Benz, L. (2014). Surface and stability characterization of a nanoporous ZIF-8 thin film. *Journal of Physical Chemistry C, 118*, 14449–14456. https://doi.org/10.1021/jp5041053
37. Angela, S., Lunardi, V. B., Kusuma, K., Soetaredjo, F. E., Putro, J. N., Santoso, S. P., Angkawijaya, A. E., Lie, J., Gunarto, C., Kurniawan, A., & Ismadji, S. (2021). Facile synthesis of hierarchical porous ZIF-8@TiO_2 for simultaneous adsorption and photocatalytic decomposition of crystal violet. *Environ. Nanotechnol. Monit. Manag., 16*, Article 100598. https://doi.org/10.1016/j.enmm.2021.100598
38. Zhang, M., Shang, Q., Wan, Y., Chengi, Q., Liao, G., & Pan, Z. (2019). Self-template synthesis of double-shell TiO_2@ZIF-8 hollow nanospheres via sonocrystallization with enhanced photocatalytic activities in hydrogen generation. *Applied Catalysis B: Environment and Energy, 241*, 149–158. https://doi.org/10.1016/j.apcatb.2018.09.036
39. Yurtsever, H. A., & Çetin, A. E. (2012). Fabrication of ZIF-8 decorated copper doped TiO2 nanocomposite at low ZIF-8 loading for solar energy applications. *Colloids and Surfaces A: Physicochemical and Engineering Aspects, 625*, Article 126980. https://doi.org/10.1016/j.colsurfa.2021.126980
40. Schlur, L., Begin-Colin, S., Gilliot, P., Gallart, M., Carré, G., Zafeiratos, S., Keller, N., Keller, V., André, P., Greneche, J.-M., Hezard, B., Desmonts, M. H., & Pourroy, G. (2014). Effect of ball-milling and Fe-/Al-doping on the structural aspect and visible light photocatalytic activity of TiO_2 towards Escherichia coli bacteria abatement. *Materials Science and Engineering C, 38*, 11–19. https://doi.org/10.1016/j.msec.2014.01.026
41. Shi, N., Li, X., Fan, T., Zhou, H., Ding, J., Zhang, D., & Zhu, H. (2011). Biogenic N-I-codoped TiO_2 photocatalyst derived from kelp for efficient dye degradation. *Energy & Environmental Science, 4*, 172–180. https://doi.org/10.1039/C0EE00363H
42. Ökte, A. N., Karamanis, D., & Tuncel, D. (2014). Dual functionality of TiO_2-flyash nanocomposites: Water vapor adsorption and photocatalysis. *Catalysis Today, 230*, 205–213. https://doi.org/10.1016/j.cattod.2014.01.031
43. Hou, F., Gorthy, R., Mardon, I., Tang, D., & Goode, C. (2022). Low voltage environmentally friendly plasma electrolytic oxidation process for titanium alloys. *Science and Reports, 12*, 6037. https://doi.org/10.1038/s41598-022-09693-w
44. Jian, M., Liu, B., Zhang, G., Liu, R., & Zhang, X. (2015). Adsorptive removal of arsenic from aqueous solution by zeolitic imidazolate framework-8 (ZIF-8) nanoparticles. *Colloids and Surfaces A: Physicochemical and Engineering Aspects, 465*, 67–76. https://doi.org/10.1016/j.colsurfa.2014.10.023
45. Shende, T. P., Bhanvase, B. A., Rathod, A. P., Pinjari, D. V., & Sonawane, S. H. (2018). Sonochemical synthesis of Graphene-Ce-TiO2 and Graphene-Fe-TiO_2 ternary hybrid photocatalyst nanocomposite and its application in degradation of crystal violet dye. *Ultrasonics - Sonochemistry, 41*, 582–589. https://doi.org/10.1016/j.ultsonch.2017.10.024
46. Luo, F., Li, M., Liang, X., Yang, J., Wang, S., Gao, X., Zhang, Z., & Fang, Y. (2023). Self-assembled TiO_2/MOF on corrugated paper as a recyclable and efficient composite for dual-channel dye removal. *Journal of Cleaner Production, 422*, 1386679. https://doi.org/10.1016/j.jclepro.2023.138679
47. Far, H. S., Najafi, M., Hasanzadeh, M., & Rahimi, R. (2022). A 3D-printed hierarchical porous architecture of MOF@clay composite for rapid and highly efficient dye scavenging. *New Journal of Chemistry, 48*, 23351–23360. https://doi.org/10.1039/D2NJ05188E
48. Jiang, X., Xu, C., Du, J., & Wang, J. (2024). PVDF-based nanofiber membrane decorated with Z-scheme TiO2/MIL-100 (Fe) heterojunction for efficient oil/water emulsion separation and dye photocatalytic degradation. *Colloid Surface A, 688*, Article 133605. https://doi.org/10.1016/j.colsurfa.2024.133605
49. Ho, Y. S., & McKay, G. (1999). Pseudo-second order model for sorption processes. *Process Biochemistry, 34*, 451–465.
50. Xu, Y., Jin, J., Li, X., Han, Y., Meng, H., Wu, J., & Zhang, X. (2016). Rapid magnetic solid-phase extraction of Congo Red and Basic Red 2 from aqueous solution by ZIF-8@$CoFe_2O_4$ hybrid composites. *Journal of Separation Science, 39*, 3647–3654. https://doi.org/10.1002/jssc.201600630
51. Tuncel, D., & Okte, A. N. (2023). Adsorption and photoactivity performances of copper(II)–benzene-1,3,5-tricarboxylate (Cu-BTC) and zeolitic imidazolate framework (ZIF-8): Effect of humidity. *Journal of Chemical Technology and Biotechnology, 98*(98), 2925–2942. https://doi.org/10.1002/jctb.7501
52. Jing, H.-P., Wang, C.-C., Zhang, Y.-W., Wang, P., & Li, R. (2014). Photocatalytic degradation of methylene blue in ZIF-8. *RSC Advances, 4*, 54454–54462. https://doi.org/10.1039/C4RA08820D
53. Zhou, H., Wang, H., Yue, C., He, L., Li, H., Zhang, H., Yang, S., & Ma, T. (2024). Photocatalytic degradation by TiO_2-conjugated/

coordination polymer heterojunction: Preparation, mechanisms, and prospects. *Applied Catalysis B, 344*, Article 123605. https://doi.org/10.1016/j.apcatb.2023.123605

54. Wei, Y., Cheng, G., Xiong, J., Xu, F., Chen, R., Li, P., Zhang, X., Hou, C., Chen, Y., & He, T. (2018). Highly efficient visible-light driven solar-fuel production over tetra(4-carboxyphenyl)porphyrin iron(III) chloride using CdS/Bi_2S_3 heterostructure as photosensitizer. *Applied Catalysis, B: Environmental, 238*, 656–663. https://doi.org/10.1016/j.apcatb.2018.07.066
55. Alvaro, M., Carbonell, E., Ferrer, B., Llabrés Xamena, F. X., & Garcia, H. (2007). Semiconductor behavior of a metal-organic framework (MOF). *Chemistry A European Journal, 13*, 5106–5112. https://doi.org/10.1002/chem.200601003
56. Zhong, W. L., Li, C., Liu, X. M., Bai, X. K., Zhang, G. S., & Lei, C. X. (2020). Liquid phase deposition of flower-like TiO_2 microspheres decorated by ZIF-8 nanoparticles with enhanced photocatalytic activity. *Micropor. Mesopor. Mater., 306*, Article 110401. https://doi.org/10.1016/j.micromeso.2020.110401